

Optical Engineering

SPIEDigitalLibrary.org/oe

Long-wave type-II superlattice detectors with unipolar electron and hole barriers

Eric A. DeCuir, Jr.
Gregory P. Meissner
Priyalal S. Wijewarnasuriya
Nutan Gautam
Sanjay Krishna
Nibir K. Dhar
Roger E. Welser
Ashok K. Sood



Long-wave type-II superlattice detectors with unipolar electron and hole barriers

Eric A. DeCuir, Jr.
Gregory P. Meissner
Priyalal S. Wijewarnasuriya
U.S. Army Research Laboratory
2800 Powder Mill Road
Adelphi, Maryland 20783
E-mail: eric.a.decuir.civ@mail.mil

Nutan Gautam
Sanjay Krishna
University of New Mexico
Center for High Technology Materials
Department of Electrical and Computer
Engineering
1313 Goddard Street SE
Albuquerque, New Mexico 87106

Nibir K. Dhar
Defense Advanced Research Projects Agency
Microsystems Technology Office
675 North Randolph Street
Arlington, Virginia 22203

Roger E. Welser
Ashok K. Sood
Magnolia Optical Technologies, Inc.
52-B Cummings Park Suite 314
Woburn, Massachusetts 01801

1 Introduction

Electro-optic and infrared (EO/IR) sensors are being developed and deployed for a wide variety of military systems applications that include but are not limited to special operation missions that call for situational awareness at a covert level. To meet the ever-increasing demands for next-generation imaging systems which include higher operating temperatures and reduced size, weight, and power, a number of technologies are readily deployed for the visible, short-wave infrared (SWIR), mid-wave infrared (MWIR), and long-wave infrared (LWIR) spectral bands.¹ These imaging systems maintain a diverse grouping of materials that excel in their individual categories, or more specifically, in their respective spectral bands where their properties make them ideal candidates. For example, InGaAs-based IR focal plane array (FPA) technologies are commonly used for SWIR sensors that operate in the 1.0 to 1.8 μm band, while InSb-based FPAs tend to dominate as MWIR sensors in the 3 to 5 μm band.² For the 8 to 14 μm LWIR band, sensor technologies include $\text{Hg}_{1-x}\text{Cd}_x\text{Te}$ (MCT), microbolometers, and Type-II superlattices (SLS).³

In addition to the aforementioned materials and extrinsic materials such as Si, quantum engineering of heterostructures such as quantum wells and superlattices have evolved

Abstract. The performance of a long-wave infrared type-II InAs/GaSb superlattice photodetector with a 50% cut-off wavelength of approximately 8.7 μm is presented. The ability to lower dark current densities over traditional P-type-Intrinsic-N-type diodes is offered by way of hetero-structure engineering of a pBiBn structure utilizing superlattice *p*-type (*p*) and *n*-type (*n*) contacts, an intrinsic (*i*) superlattice active (absorber) region, and unipolar superlattice electron and hole blocking (B) layers. The spectral response of this pBiBn detector structure was determined using a Fourier transform infrared spectrometer, and the quantum efficiency was determined using a 6250 nm narrow band filter and a 500 K blackbody source. A diode structure designed, grown, and fabricated in this study yielded a dark current density of 1.05×10^{-5} A/cm² at a reverse bias of -50 mV and a specific detectivity value of greater than 10^{11} Jones at 77 K. Theoretical fittings of the diode dark currents at 77 K were used in this study to help isolate the contributing current components observed in the empirical dark current data. A variable temperature study (80 to 300 K) of the dark current is presented for a diode demonstrating diffusion-limited dark current down to 77 K. © 2012 Society of Photo-Optical Instrumentation Engineers (SPIE). [DOI: [10.1117/1.OE.51.12.124001](https://doi.org/10.1117/1.OE.51.12.124001)]

Subject terms: type-II; InAs/GaSb; strained-layer superlattice; superlattices; pBiBn; infrared; dark current; photodetectors.

Paper 121399P received Sep. 25, 2012; revised manuscript received Nov. 1, 2012; accepted for publication Nov. 2, 2012; published online Dec. 3, 2012.

greatly since first proposed more than four decades ago by Esaki and Tsu.^{4,5} Building upon this proposed idea and the power of the mature III-V industry, the quantum well infrared photodetector (QWIP) was born,⁶ and has since become well-positioned as a mainstream technology for LWIR sensors. In recognition of the success and short-comings of AlGaAs/(In)GaAs QWIP technology, the research community has witnessed a large push towards investigating other III-V technologies such as InAs/(In)GaSb type-II SLS materials for their theoretical ability to outperform existing technologies such as MCT⁷ and their anticipated ability to compete at a lower cost. The fabrication of large-format FPAs from type-II SLS is believed to offer specific advantages over the competing MCT technology. These advantages include the maturity of III-V processing technology; improved bandgap tunability over a large range ($\sim 2\text{--}25$ μm) due to precise molecular beam epitaxy (MBE) thickness control of the epitaxial layers; reduced tunneling due to the larger; bandgap-independent effective mass (electron and hole); and reduced Auger recombination due to strain-induced splitting of heavy hole and light hole bands.⁸

The suppression of dark current in type-II SLS devices via heterostructure engineering of unipolar barriers on each side of the absorber region is presented herein. This structure, hereafter defined as a pBiBn architecture, consists of an *n*-contact layer followed by a hole-blocking layer "B" and then the intrinsic absorber region "i," which is followed

by an electron blocking layer “B” and finally a *p*-contact layer. The addition of the hole and electron barriers flanking both sides of the absorber region serves to drop most of the voltage and produce a low electric-field absorber region. This effect leads to reduced dark current as a result of reduced tunneling and Shockley-Read-Hall (SRH) recombination currents in the active region. In addition, these barriers also serve to lower diffusion currents by blocking the minority carriers from either side of the junction.

This paper will first begin by describing the details of the growth and processing methods and then focus on the optical and electrical characterization of these samples at cryogenic temperatures.

2 Methodology

2.1 MBE Growth Details

The material in this study was grown at the University of New Mexico on Te-doped, epi-ready, (100) GaSb substrates using a VG80 solid source molecular beam epitaxy (MBE) system. This system was equipped with SUMO® cells for gallium and indium, a standard effusion cell for aluminum, and cracker cells for antimony and arsenic. The growth rates in this study were calibrated by monitoring the reflected high-energy electron diffraction (RHEED) intensity oscillations arising from the layer-by-layer growth mode. To further validate the accuracy of this technique, high resolution x-ray diffraction (XRD) was used to confirm the periodicity of calibration superlattices (SL) with different SL periods. The grown pBiBn design shown in Fig. 1 consists of an 800 nm thick *n*-type contact layer made of a 9 monolayer (ML) InAs/4 ML GaSb superlattice doped with Te ($n = 3 \times 10^{18} \text{ cm}^{-3}$) followed by a 275 nm thick nonintentionally doped (n.i.d) *p*-type $\sim ([5-10] \times 10^{14} \text{ cm}^{-3})$ hole blocking layer made of 16 ML InAs/4 ML AISb SLS. This is followed by a 1.94 μm thick n.i.d absorber region *p*-type $\sim (1 \times 10^{16} \text{ cm}^{-3})$ comprised of 14 ML InAs/7 ML GaSb SLS and a 149 nm thick n.i.d electron blocking layer, *n*-type $\sim ([8-10] \times 10^{14} \text{ cm}^{-3})$ formed from 7 ML GaSb/4 ML AISb SLS. The top cap layer consists of a 130 nm thickness of

5 ML InAs/8 ML GaSb SLS *p*-contact layer doped with Be ($p \sim 2.8 \times 10^{18} \text{ cm}^{-3}$).

2.2 Sample Preparation/Processing

The samples in this study were diced into approximately 1 cm^2 pieces and cleaned using a basic degreasing procedure involving three individual soaks in acetone, methanol, and isopropanol (IPA) for 3 min, respectively. Prior to the degreasing soaks, the samples were exposed to a high-pressure acetone jet-spray to remove any stubborn organics or particulates remaining on the surface from dicing. Following the final 3-min IPA soak and deionized (DI) water rinse, the samples were dried under a stream of dry nitrogen. Finally, a 60 s dehydration bake at 110°C was performed preceding the application of AZ 5214E photoresist (PR).

Using a standard lithography procedure with AZ 5214E PR, samples were patterned with a variable area mesa mask to define different mesa structures for subsequent dry etching. Following exposure and development of the 1.5 μm thick PR layer, samples then were loaded in a March Plasma barrel etcher for a 2 min cleaning cycle to ensure complete removal of any minor PR residue remaining on the surface after patterning. Dry etching was performed in a Unaxis Versaline inductively coupled plasma (ICP) system using an optimized BCl_3 etch to achieve relatively smooth sidewall morphology and excellent selectivity with our AZ 5214E PR mask. The sample was mounted onto a 4-inch Si carrier wafer using Cool-Grease™ CGR7016 to enhance thermal conductivity between the sample piece and the helium cooled wafer chuck. The temperature of the sample was held at 25°C to avoid burning of the photoresist during extended etching. The forward reactive ion etching (RIE) and inductively coupled plasma (ICP) powers were set at 150 and 500 W, respectively. The chamber pressure was held at 3.2 mTorr with a BCl_3 flow of 32 sccm (standard cubic centimeter per minute), which resulted in an etch rate of approximately 120 nm/min, a final etch depth of 2.7 μm , and a sidewall angle of approximately 75 deg.

After etching, the samples were briefly wet-etched in a $\text{H}_3\text{PO}_4:\text{H}_2\text{O}_2:\text{H}_2\text{O}:\text{Tartrate}$ (30:30:90 ml:5 gr) solution

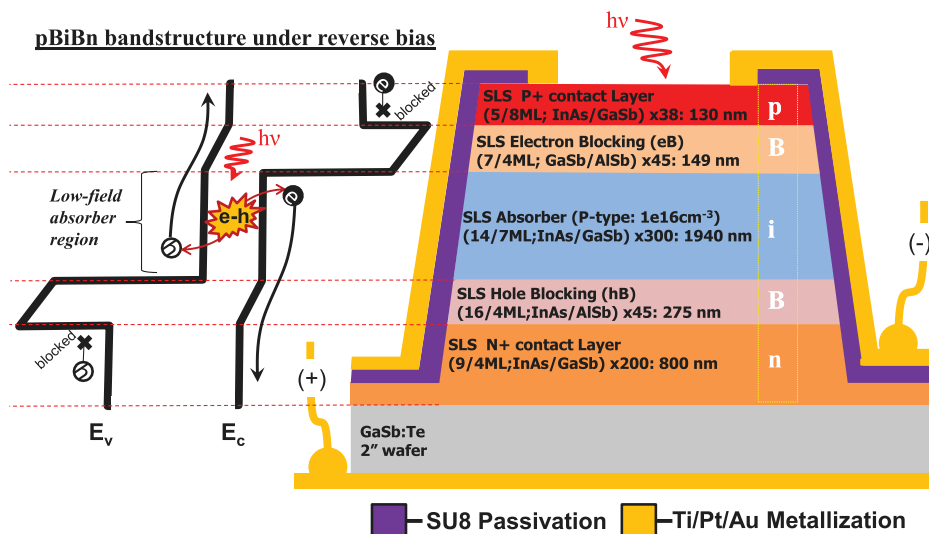


Fig. 1 Conceptualization of the pBiBn band-structure under reverse bias (left) and illustration of the layer-by-layer cross-section of the processed diode structure (right).

diluted with H₂O 1:2 for 10 s to remove any dry etch damage from the mesa sidewalls and surface. The samples were immediately soaked in acetone for 5 min to strip the remaining PR from the sample surface, rinsed with flowing acetone and IPA, respectively, and lastly dried under a stream of dry nitrogen. The samples were then loaded into a PM-600 March Plasma barrel etcher for 120 s oxygen clean to remove any remaining organics from the surface of the sample. Following the last cleaning step in the barrel etcher, the native surface oxide layer formed during the organic plasma clean and atmospheric exposure was removed by dipping the samples in a 10% weight/volume HCl solution for 60 s. Directly upon removal from the HCl solution, the sample was rinsed with isopropanol, dried under a stream of nitrogen gas, and immediately coated with a 1.5 μm thick layer of SU8-2 to passivate and protect the surface from further oxidation. Metal contact vias were lithographically opened using a standard SU8-2 lithography procedure and made permanent by baking the SU8-2 layer for 5 min at 150°C on a hotplate.

Finally, using a standard lithography procedure with AZ 5214E PR, SU8 patterned samples were again patterned with a variable area metal mask to form ring contacts on the top of the etched mesa and at off-mesa wire bonding pads. Prior to loading into the e-beam evaporation system, samples were again treated with an HCl:H₂O solution to remove any native oxide, dried under a stream of dry nitrogen, and immediately loaded into the e-beam evaporator. A standard ohmic contact metallization of Ti/Pt/Au was deposited using a multiple-pocket e-beam evaporator at a base pressure of less than 1×10^{-6} Torr. Following contact deposition, metal lift-off was performed in acetone with the aid of gentle pipette agitation. The aforementioned cleaning procedure was then repeated and samples were mounted and wire-bonded in a 68-pin carrier for testing.

2.3 Characterization Details

Packaged samples were subsequently loaded into a pour-fill Lakeshore modular test dewar (MTD125) with individually shielded coaxial break-outs for each wire-bonded device. The dewar was equipped with a 2-inch ZnSe window yielding approximately 70% transmission over the spectral range of approximately 1 to 12 μm. The limiting cold-stop aperture in these experiments provided an $f/2.7$ field of view (FOV). The spectral response measurements for these devices were performed at 77 K using a Nicolet 8700 Fourier transform infrared (FTIR) spectrometer in conjunction with a low-noise Keithley 428 transimpedance preamplifier.

All radiometric measurements were carried out using the MTD125 dewar outfitted with a cold Spectragon® narrow band-pass filter with a center wavelength at 6250 nm, a full width half maximum of 95 nm, and average transmission of 58% (blocking from 0.1 to 30 μm). The calibrated flux density was delivered by a chopped, 500 K cavity blackbody mounted a fixed distance from the device under test (DUT). The chopped device photocurrent signal was fed into a Stanford Research Systems SRS SR830 digital lock-in amplifier to determine the root-mean square device current amplitude based on the difference of the chopped level of radiation. This information, in addition to the form factor of the blackbody chopper, allowed the calculation of the external quantum efficiency. An HP3580A spectrum analyzer was used to determine the noise current spectral density (A/\sqrt{Hz}), from

which in conjunction with the measured photocurrent, the specific detectivity is calculated. Dark and illuminated current-voltage (I-V) characteristics were determined for the devices at various temperatures using a HP4156 semiconductor parameter analyzer equipped with high resolution source measurement units (HRSMU) capable of resolving currents down to the fA level.

3 Results and Discussion

3.1 Device Operation

The layer-by-layer structure details previously described in Sec. 2.1 are shown in Fig. 1. To help visualize the expected band structure from this growth sequence, a conceptualization of it is also provided in the figure showing the device's expected mode of operation under illumination and reverse bias. It has been previously shown that the pBiBn design offers improved dark current performance over an equivalent P-type-Intrinsic-N-type (PIN) diode structure lacking hole and electron blocking layers.⁹⁻¹¹ A PIN diode's dark current primarily originates from minority carrier diffusion, tunneling, SRH, and thermally generated currents. The pBiBn structure is designed to screen these current contributions via electron and hole barriers with bandgap engineering of constituent materials. Since this structure is entirely composed of superlattice material, ultimate tunability is achieved by tailoring band-offsets to achieve optimal performance. For instance, the wider bandgap electron barrier shown in Fig. 1 has been designed to provide a barrier from minority carrier (e^-) diffusion from the p -type layer into the absorber region, yet allowing unimpeded flow of holes from the active region to the p -type contact during reverse bias operation. A similar benefit is received for the complementary hole blocking layer. These barriers also allow a large part of the electric field to drop across the wider bandgap barrier materials, which in turn reduces dark current associated with generation-recombination (G-R) currents, tunneling currents, and the activity of SRH centers in the absorber region.

3.2 Spectral Characterization

The normalized spectral response (per watt) for a pBiBn diode with a 50% cut-off of 8.65 μm is shown in Fig. 2(a) (L11-109 is designated sample used in this study). To determine the per-watt spectral shape, the single beam FTIR spectrum of the pBiBn structure was collected and then divided by the single beam FTIR spectrum of a deuterated triglycine sulfate (DTGS) reference detector. This technique is facilitated by the "spectrally flat" nature of the pyroelectric DTGS detector. However, to get the correct spectral shape, the frequency-dependent gain of the DTGS must be characterized to compensate for the FTIR modulation frequency at each wavelength. From this technique, the true per-watt spectral shape of the DUT was derived, improving its qualities as a spectral reference. The dark and light I-V characteristics of a 100 μm diode are shown in Fig. 2(b). This measurement was taken with the diode shuttered with a 77 K cold shield and in the presence of unfiltered, broadband, 300 K background radiation under an $f/2.7$ FOV. At -50 mV reverse bias, the dark current density of this diode is approximately 1.05×10^{-5} A/cm² and the induced photocurrent due to a 300 K background is 1.38×10^{-4} A/cm², which is 13 times higher than the zero FOV dark current.

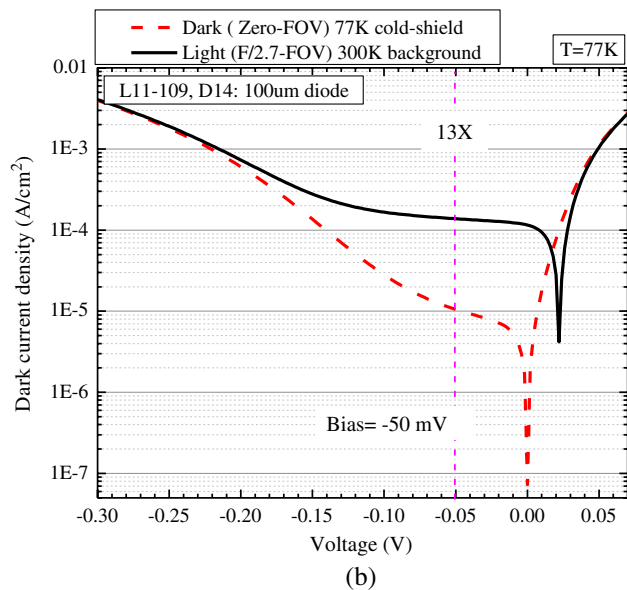
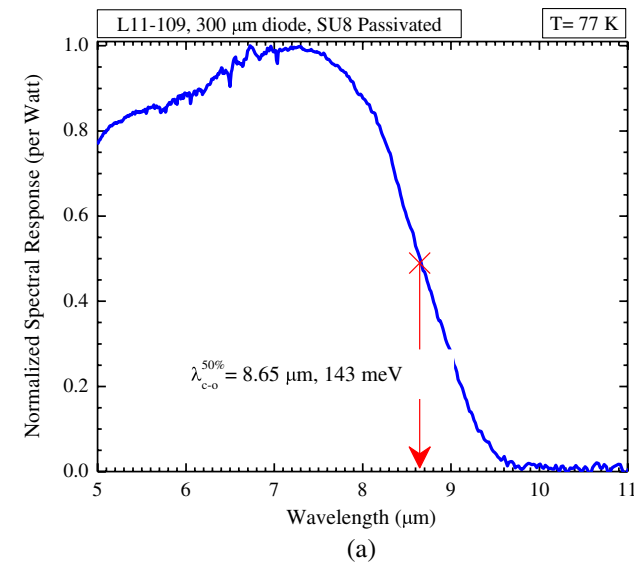


Fig. 2 (a) Normalized FTIR spectral response (per watt) from pBiBn structure. (b) Dark current and photocurrent of 100 μm diode at 77 K with a zero and F/2.7 FOV looking at a 77 K cold-shield and a 300 K background, respectively.

The quantum efficiency of the detector shown in Fig. 3 versus reverse bias was measured using the setup described in Sec. 2.3. The external quantum efficiency (QE) is shown to be enhanced as reverse biases are increased up to -150 mV where it peaks (at ~ 6.25 μm) at 23.6%. The increased bias needed to operate this device lends evidence to the presence of an unintended valence band barrier that must be overcome with an appreciable bias before efficient flow of photo-excited carriers is possible. Additionally, the decrease in quantum efficiency beyond -150 mV is most likely associated with the rapid increase in dark current contributed from a trap-assisted tunneling component (discussed in subsequent sections) which in essence begins to swamp any perceptible photocurrent. In the future, in order to compensate for this valence band barrier, a more rigorous understanding and control of the doping levels in these barriers is needed, which is expected to reduce or eliminate this

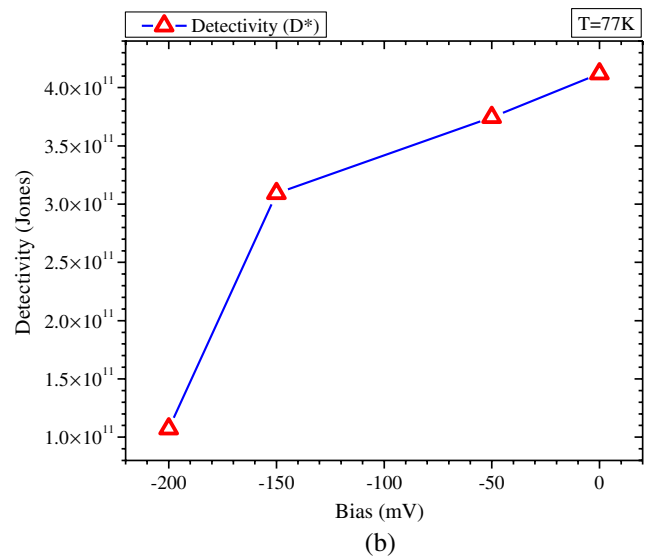
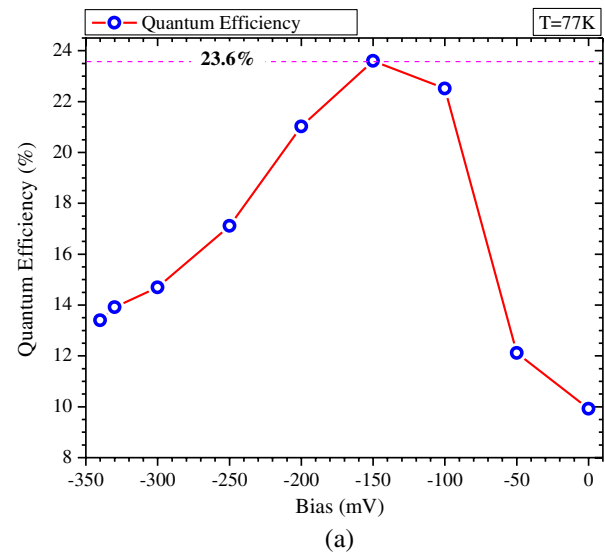


Fig. 3 (a) External quantum efficiency versus bias for a 250 μm ring diode. (b) Specific detectivity for 250 μm ring diode.

effect. However, it should also be noted that the experimental device geometry is nonideal since these samples are front-side illuminated where contact metal obscures and reflects part of the incoming flux. Therefore, for this illumination geometry, the QE is calculated based on the optical area instead of the junction area assuming that photo-generated carriers are only contributed from the direct illuminated regions. It is expected that future studies with an improved device layout and/or with backside illumination may yield a more direct representation of the QE. The specific detectivity was calculated for four different biases by measuring the noise current spectral density at each bias; these are plotted in Fig. 3(b). The specific detectivity (D^*) was calculated using the following expression:

$$D^* = \frac{\mathfrak{R} * \sqrt{A_d}}{S_N} \left[\text{cm} \frac{\sqrt{\text{Hz}}}{\text{W}} \text{ or Jones} \right], \quad (1)$$

where \mathfrak{R} is the responsivity, A_d is the detector area, and S_N is noise current spectral density ($\text{A}/\sqrt{\text{Hz}}$).

At the peak QE, the measured noise of 61 fA (at 100 Hz) is in good agreement with the theoretically calculated noise of 46 fA, which yielded the specific detectivity of 3.1×10^{11} Jones at 100 Hz. The decrease in D^* with larger reverse bias is attributed to a marked increase in measured noise which is consistent with the large increase of dark current. This rapid increase in dark current is attributed to a large tunneling component that will be analyzed and discussed in the following sections.

3.3 Dark Current Characterization

The dark current densities of variable area diodes (40, 100, and 200 μm) at 77 K are shown in Fig. 4(a). One may notice that the dark current densities vary greatly among the three diodes. To better understand and explain the origin of these dark current variations, a theoretical current fitting routine was used to model the 77 K currents in an effort to explain the disparity between the observed dark current behaviors in these photovoltaic diodes. The theoretical fitting allows one to account for the dominant currents that are contributing to the summed total current observed in the experimental

measurements. The equations used to model the currents in a photovoltaic diode are summarized in recent papers.^{12,13} The theoretical fit herein takes into account the contributions of diffusion, G-R, shunt, and trap-assisted tunneling currents to obtain a best fit to the empirical data in the given data range. The dark current for each diode was empirically fit in the given range shown in Fig. 4(b)–4(d), since the data outside of this range does not lend itself to accurate fitting within our current model. That is, outside of this range, the device appears to be affected by band-to-band tunneling or premature diode breakdown, both beyond the scope of the fitting model used for this analysis. Nevertheless, the devices have been reasonably well characterized in the given range and one may surmise the dominant current components contributing to the dark current data for three diodes shown in Fig. 4(b)–4(d). Overall, the 100 μm device yielding the best performance appears to have roughly an order of magnitude higher shunt resistance ($3.5 \times 10^8 \Omega$) than the 40 and 200 μm counterparts, which is best fit with shunt resistances in the range of $(1\text{--}2) \times 10^7 \Omega$. All the devices apparently suffer from some trap-assisted tunneling mechanism, which

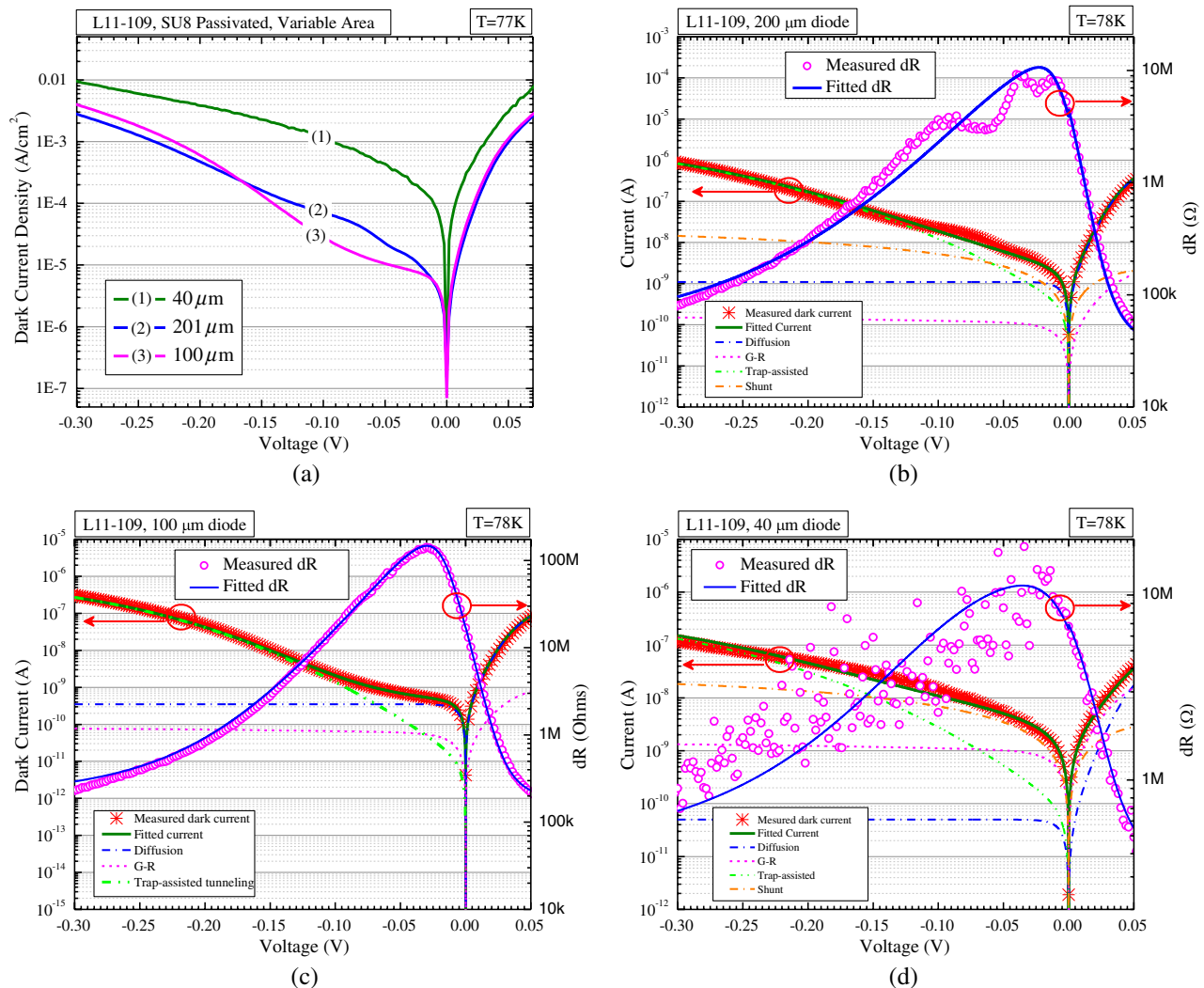


Fig. 4 (a) Dark current density from three differently sized diodes processed and passivated with SU8-2 from L11-109 material (pBiBn sample). (b) Theoretical current fitting for 200 μm diode, (c) 100 μm diode, and (d) 40 μm diode taking into account diffusion, generation-recombination (G-R), shunt, and trap-assisted tunneling currents. The associated differential resistance (dR) is also shown and fitted with the extrapolated dR from the theoretical current fit.

adversely affects the performance at larger reverse biases. However, this tunneling effectively explains the observed current behavior and the perceived roll-off from peak dynamic resistance.

It is believed that the source of this low shunt resistance in the 40 and 200 μm diodes could ultimately be the result of poor or inadequate surface passivation with the SU8-2 material. In this study, SU8-2 photoresist was used to permanently passivate the diode sidewalls and surface, principally due to its ease and speed of deposition. However, one cannot confidently discount the increased probability of capturing a defect in the larger 200 μm diode. Overall, it is well understood that surface passivation becomes increasingly important in long-wave devices and also as diode sizes get smaller.¹⁴ This in itself drives the need for the development of a more robust passivation scheme that effectively eliminates the formation of conductive oxides so that the surface resistivity can be increased and that minimizes the incorporation of trapped interfacial charges which have been known to contribute to surface channel currents.¹⁵

To gain further insight into the dark current-voltage behavior of these three diodes, the results of a temperature-dependent study shown in Fig. 5(a)–5(c) were used to further evaluate the dominant current mechanisms contributing to the dark current over the range of 77 to 300 K. The symbol size was selected to represent a potential temperature error of ± 2.5 K. While there is no expectation for the temperature diode to have an error of more than 0.1 K, the thermal transfer rate between the tip of the cold head (location of temperature sensor) and the LCC is expected to result in some temperature differential when sweeping through temperatures since only mechanical contact is utilized. It is understood that the dynamic-impedance area at zero bias (R_0A) follows an exponential dependence that is proportional to $\exp(-E_g/kT)$, where E_g is the bandgap energy, if the diode is in a diffusion-limited regime and follows an exponential dependence that is proportional $\exp(-E_g/2kT)$ if the diode is in a generation-recombination (G-R) limited regime. This relationship stems from the fact that an ideal photodiode with a lightly doped p -type absorber has the current density (J_d) as follows:

$$J_d = \frac{qn_i^2 L_e}{N_A \tau_e} [\exp(qV/kT) - 1], \quad (2)$$

where q is the electron charge, n_i is the intrinsic carrier concentration, τ_e is the minority electron lifetime, N_A is the p -type impurity concentration, and L_e is electron the diffusion length. Since the dark current density is proportional to the intrinsic carrier concentration, which increases exponentially with decreasing E_g , one may use this relationship to perform an Arrhenius analysis of the activation energy over those select temperature ranges. This dependence on n_i was also established by Mou et al.¹⁵ in the case of a surface channel current where the R_0A is shown to be proportional to $n_i^{0.5}$. Based on this, one can expect an Arrhenius plot of R_0A versus $1/kT$ to yield data whose slope is related to the dominant current mechanism which is in turn related to the material's bandgap and passivation through the exponential of E_g/n , where n is 1 for diffusion, 2 is for G-R, and greater than 2 to 4 is for the surface channel case.

A similar temperature-dependent analysis may be performed at a particular device voltage to gather additional information about the performance at that bias. This type of analysis, hereafter deemed a dynamic impedance-area analysis ($R_{\text{eff}}A$), at a particular bias and temperature is expected to yield similar information given that the aforementioned justification for R_0A also holds true for $R_{\text{eff}}A$. The analysis for R_0A for this data was previously reported in DeCuir et al.¹⁶ For the $R_{\text{eff}}A$ analysis, the effective dynamic impedance-area product at -50 mV was determined using the following relationship:

$$R_{\text{eff}}A = \frac{kT}{q * J(-50 \text{ mV})}, \quad (3)$$

where k is Boltzmann's constant, T is the temperature, q is the electron charge, and $J(-50 \text{ mV})$ is the current density at -50 mV.

The effective dynamic impedance-area product ($R_{\text{eff}}A$, $V_b = -50$ mV) versus temperature was evaluated for each diode and plotted versus $1/kT$ in Fig. 5(a)–5(c) to determine the activation energy from the slope and to relate this to the 50% cut-off energy, i.e., approximate to the bandgap ($E_g \sim 143$ meV) of the material in this study. As seen in Fig. 5(a) and 5(b), the data trended closely with a diffusion-limited behavior from ~ 150 K down to 80 K. The temperature dependence data for the 40 μm diode shown in Fig. 5(c) yielded similar behavior in the higher temperature

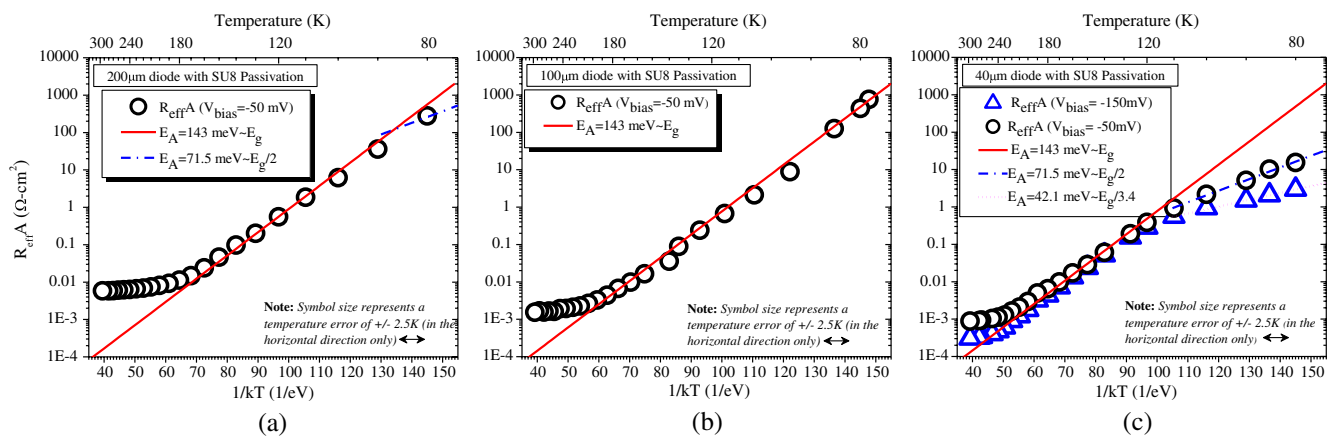


Fig. 5 $R_{\text{eff}}A$ ($V_{\text{bias}} = -50$ mV) versus $1/kT$ data for (a) 200 μm diode, (b) 100 μm diode, and (c) 40 μm diode. $R_{\text{eff}}A$ ($V_{\text{bias}} = -50$ mV) versus $1/kT$ is also presented in (c).

range, but diverged from the diffusion line below 110 K and began to follow a G-R limited line. In Fig. 5(c), the $R_{\text{eff}}A$ at a bias of -150 mV is also presented to illustrate the transition from what appears to be a G-R dominated regime at low temperature (surface G-R) to what appears to be a surface channel current dominated regime which yields a slope that is in the range of $E_g/3.4$. In all the diodes, temperature-dependent data in Fig. 5(a)–5(c) show that there was also an unexpected saturation of the $R_{\text{eff}}A$ at higher temperatures causing the data to deviate from the expected diffusion-limited regime. Closer observation of the high temperature data among all three diodes also revealed a relationship to the diode size and thus apparent deviation from the diffusion line. Specifically, it appears that the onset of this deviation at higher temperatures becomes more pronounced as the size of the device is increased. Primarily, the largest device is most affected by this phenomenon, leading to a deviation from the diffusion trend beginning at approximately 160 K. A previous report in the literature presents a possible explanation linking this phenomenon to the device geometry and structure. This effect has been previously documented in similar barrier device structures where current localization occurs in these barrier structures due to a nonuniform electric potential, which in effect leads to a two-dimensional type transport regime at higher temperatures.¹⁷ This current localization or electric nonuniformity essentially arises from current spreading due to the device geometry that was employed in this study. Given the fact that these devices are contacted by a small metal ring along the edge of each diode as seen in Fig. 1, the electric potential under the edge metal contact region becomes greater than the potential at the center of the ring. In order to realize uniform currents, the carriers must move quickly to the edge contacts. In effect, this nonuniformity creates reduced collection efficiency on carriers, consequently also reducing the detector response. Additionally, as the temperature is increased, the rate of thermionic emission of carriers over the barrier also increases, which compounds the problem of uniform currents and collection efficiency. Furthermore, this current nonuniformity is shown to be more prominent with increased device size, which is confirmed in the data presented here.¹⁷

4 Conclusion

A LWIR pBiBn type-II superlattice diode yielding a cut-off of $8.7 \mu\text{m}$ was investigated. It was shown that dark current densities could be managed using hetero-engineered electron and hole blocking layers. With this design, dark current densities were shown to be below 0.01 mA/cm^2 at a reverse bias of -50 mV and a device was shown to produce a specific detectivity value of 3.7×10^{11} Jones at 77 K at a reverse bias of -50 mV. Although modest quantum efficiency data were presented, the device geometry employed in this study proved to be nonideal for front-side illumination and the employed contact geometry. Theoretical fitting of the dark current for three different sized diodes revealed the presence of large trap-assisted tunneling currents at larger bias and reduced shunt resistances in two of the devices leading to increased currents and reduction of the dynamic impedance. In the temperature dependent $R_{\text{eff}}A$ study, it was revealed that while the larger 100 and $200 \mu\text{m}$ devices displayed diffusion limited behavior down to 77 K, the $40 \mu\text{m}$ device exhibited a deviation from diffusion to G-R limited behavior

for temperatures below 110 K, which was shown to potentially be linked to surface G-R at -50 mV and surface channel currents at -150 mV. In addition, it was also shown that irregular $R_{\text{eff}}A$ diode behavior occurred at higher temperatures due to the ring contact geometry that resulted in current nonuniformities. It is believed that further studies involving variable area diode analysis (VADA) will be needed to fully characterize the diode sidewall resistivity. On the whole, it is believed that this future VADA study may help isolate the origin of these large tunneling and shunt currents, whether surface or bulk related.

References

1. H. Pollehn et al., "IR material research at the Army Research Laboratory," *Proc. SPIE* **6542**, 65420C (2007).
2. H. Yuan et al., "FPA development: from InGaAs, InSb, to HgCdTe," *Proc. SPIE* **6940**, 69403C (2008).
3. P. W. Norton et al., "Commercialization of uncooled infrared technology," *Proc. SPIE* **5563**, 55–61 (2004).
4. L. Esaki and R. Tsu, "Superlattice and negative differential conductivity in semiconductors," *IBM J. Res. Dev.* **14**(1), 61–65 (1970).
5. K. K. Choi et al., "Corrugated quantum-well infrared photodetector focal plane arrays," *IEEE J. Quantum Electron.* **45** (10), 1255–1264 (2009).
6. B. F. Levine et al., "New $10 \mu\text{m}$ infrared detector using intersubband absorption in resonant tunneling GaAlAs superlattices," *Appl. Phys. Lett.* **50**(16), 1092–1094 (1987).
7. C. H. Grein, P. M. Young, and H. Ehrenreich, "Minority carrier lifetimes in ideal InGaSb/InAs superlattices," *Appl. Phys. Lett.* **61**(24), 2905–2907 (1992).
8. C. H. Grein et al., "Auger recombination in narrow-gap semiconductor superlattices incorporating antimony," *J. Appl. Phys.* **92**(12), 7311–7316 (2002).
9. N. Gautam et al., "Performance improvement of longwave infrared photodetector based on type-II InAs/GaSb superlattices using unipolar current blocking layers," *Appl. Phys. Lett.* **96**(23), 231107 (2010).
10. E. A. Plis et al., "Performance of long-wave infrared InAs/GaSb strained layer superlattice detectors for the space applications," *Proc. SPIE* **8164**, 81640S (2011).
11. B.-M. Nguyen et al., "Background limited long wavelength infrared type-II InAs/GaSb superlattice photodiodes operating at 110 K," *Appl. Phys. Lett.* **93**(12), 123502 (2008).
12. P. S. Wijewarnasuriya et al., "High-performance long-wavelength infrared HgCdTe focal plane arrays fabricated on CdSeTe compliant Si substrates," *IEEE Trans. Electron Devices* **57**(4), 782–787 (2010).
13. V. Gopal et al., "Modeling of electrical characteristics of midwave type II InAs/GaSb strain layer superlattice diodes," *J. Appl. Phys.* **104**(12), 124506 (2008).
14. E. A. DeCuir, Jr., J. W. Little, and N. Baril, "Addressing surface leakage in type-II InAs/GaSb superlattice materials using novel approaches to surface passivation," *Proc. SPIE* **8155**, 815508 (2011).
15. S. Mou, J. V. Li, and S. L. Chuang, "Surface channel current in InAs/GaSb type-II superlattice photodiodes," *J. Appl. Phys.* **102**, 066103 (2007).
16. E. A. DeCuir, Jr. et al., "Design and development of low dark current SLS detectors for IRFPA applications," *Proc. SPIE* **8512**, 85120N (2012).
17. Y. F. Lao et al., "Analysis of dark current mechanisms for split-off band infrared detectors at high temperatures," *IEEE Trans. Electron Devices* **57**(6), 1230–1236 (2010).



Eric A. DeCuir Jr. is currently a research physicist in the EO/IR division at the U.S. Army Research Laboratory in Adelphi, Maryland. His current research focuses on photonic and electronic properties of HgCdTe and Type II GaSb/InAs superlattice materials as well as focal plane array characterization. His research efforts have spanned material systems such as III-nitride, III-V, and II-VI materials systems for studying bulk and quantum confined properties of superlattices, quantum wells, quantum wires, and quantum dot structures. His education includes a bachelor's degree in electrical engineering from the University of Louisiana at Lafayette and a MS and PhD in microelectronics and photonics from the University of Arkansas. He has over nine years of experience with optical and electrical characterization of semiconductor materials and over seven years experience with molecular beam epitaxy growth of III-Nitride materials.



Gregory P. Meissner is an engineering technician within the II-VI Materials and Devices Team in the Electro-Optics Materials and Devices Branch of the U.S. Army Research Laboratory. He has over 33 years of semiconductor fabrication experience in various commercial and defense oriented facilities. His experience includes fabricating devices and detectors out of various materials, including II-VI materials such as mercury cadmium telluride, III-V materials such as InAs/GaSb with superlattice structures, carbon nano-tube/graphene, organic polymers, and IR detectors using germanium and nanoparticles. He also has extensive experience in research, development, and fabrication of quantum cascade and inter-band cascade lasers.



Priyalal S. Wijewarnasuriya received his PhD in physics from the University of Illinois at Chicago and at presently leads the II-VI Materials and Devices Team at the EO/IR Materials & Devices Branch of SEDD at the U.S. Army Research Laboratory in Adelphi, Maryland. He has extensive experience in all aspects of the HgCdTe alloy system, including device modeling, designing device fabrication experiments and defect analysis. Before joining ARL, he was a member of the technical staff at the Rockwell Scientific Center, California. At Rockwell, he was a member of the team dedicated to the demonstration of novel, large-format infrared focal plane arrays for tactical and strategic military applications as well as astronomy. He has authored or co-authored over 73 papers in the open technical literature, two book chapters and has presented his work at numerous national and international conferences.



Nutan Gautam received her BS and MS degrees from Dayalbagh Educational Institute, Agra, India, in 2003 and 2005, respectively. She received the MTech degree in electrical engineering from the Indian Institute of Technology, Kanpur, India, in 2007, and PhD degree at Center for High Technology Materials, University of New Mexico, Albuquerque in 2012. She is currently with the Institute of Terahertz Science and Technology, University of California Santa Barbara. Her areas of interests are in optoelectronics and photonics, with specialization in epitaxial growth, fabrication and characterization of devices.



Sanjay Krishna is a professor and regents lecturer of Electrical and Computer Engineering at the University of New Mexico's (UNM) Center for High Technology Materials. UNM named him the Regents' Lecturer (2009) and Teacher of the Year (2010) in recognition of his extraordinary accomplishments and leadership in teaching, research, and service. He has authored/co-authored more than 100 peer-reviewed journal articles with over 2800 citations with an H-index of 30. He also has four book chapters and has six issued patents. He has recently been recognized as a fellow of SPIE. He earned his PhD

and master's degrees in electrical engineering at the University of Michigan at Ann Arbor in 2001. He holds two master's degrees, MSc in electrical engineering from University of Michigan in 1999, and MSc in physics from the Indian Institute of Technology in Madras in 1996.



Nibir K. Dhar joined the DARPA Microsystems Technology Office in March 2008. He is interested in developing innovative technologies in a broad field that adds value to the warfighter's objectives in the areas of novel architectures in infrared detectors and imaging, nanoelectronics including NEMS/MEMS components, novel materials synthesis techniques, bio-inspired concepts, and new modality power sources and storage. He received a master's degree and PhD in electrical engineering from the University of Maryland at College Park in the area of microelectronics and electrophysics. He received a bachelor's degree in electrical and computer engineering from George Mason University. He has authored numerous papers on various subjects, served as chairman on numerous conferences and committees, and served as co-editor of several conference proceedings. He mentored and served on eight doctoral thesis advisory committees on various subjects.



Roger E. Welsler is the chief technology officer at Magnolia Optical Technologies, where he is responsible for leading the development of next-generation photonic devices employing advanced nanostructured materials and coatings. Prior to joining Magnolia in August of 2009, he served as director of technology and new product development at Kopin Corporation, a leading manufacturer of III-V device materials and innovator in the area of nanosemiconductor materials. At Kopin, he conceived, developed, and deployed a next generation III-V transistor structure for power amplifiers in mobile phone products. He has also pioneered the development of quantum-structured solar cells and other advanced photovoltaic device designs, and was a fellow of the NASA Graduate Student Researcher's Program. He received his PhD in applied physics from Yale University in 1995 and an undergraduate BA degree with honors in physics from Swarthmore College in 1989.



Ashok K. Sood is the president and chief executive officer of Magnolia Optical Technologies. He is a 35-year industry veteran with experience that includes developing and managing optical, photovoltaic and optoelectronics technology products for several major corporations, including Lockheed-Martin, BAE Systems, Loral, Honeywell, and Tyco International. During his career, He has worked to develop ribbon silicon solar cells, as well as CdTe, CdS and HgCdTe, GaN/AlGaN, ZnO semiconductor devices. He has also led the development of optoelectronics and imaging devices for various defense applications, including EO, IR and UV imaging, secure communications, and self-protection applications. He has received his PhD and MS in engineering from the University of Pennsylvania and has an MS and a BS in physics (honors) from Delhi University in India.